Nickel nanobrush platform for a magnetic field-assisted electrochemical response enhancement

Fernando Meneses[1], Fabiana A. Gutiérrez[2], Silvia E. Urreta[1], Paula G. Bercoff[1]*, Marcela C. Rodríguez[2]

[1] Universidad Nacional de Córdoba, Facultad de Matemática, Astronomía, Física y Computación (FAMAF). CONICET, Instituto de Física Enrique Gaviola (IFEG).
[2]INFIQC, Departamento de Fisicoquímica, Facultad de Ciencias Químicas.
Universidad Nacional de Córdoba, Ciudad Universitaria, 5000 Córdoba, Argentina.

*bercoff@famaf.unc.edu.ar; marcela.rodriguez@unc.edu.ar

Abstract

A single-step electrochemical procedure to synthesize a brush-like platform (composed of a nickel nanowire array attached to a nickel continuous layer acting as a solid base, is described. Room temperature hysteresis properties of this brush-like architecture (nanobrush) and those of the individual components (nanowires and layer) are determined. It is shown that the direction of the nanobrush magnetic easy axis may be tailored, being also possible to control the magnetic system's coercivity and remanence. The electrochemical response and the catalytic activity of a Ni nanobrush towards the redox probes $[Fe(CN)_6]^{4-/3-}$ and ethanol were evaluated, in presence and absence of an applied magnetic field. The external field strongly affects the system's behavior by enhancing the electrode charge-transfer response, even at fields as low as 6 mT. This improvement was further investigated by Electrochemical Impedance Spectroscopy and Electrochemical Capacitance Spectroscopy studies. It is concluded that the enhanced electrochemical charge-transfer process of the Ni nanobrush electrode, with a magnetic field applied along the Ni nanowires axis, arises from a larger electroactive area.

PACS: 62.23.Hj, 75.30.Gw, 75.50.-y, 75.75.-c.

Keywords: Nickel nanowires; Nickel nanobrush; Nanowires' array; Magnetic anisotropy; Magnetic on/off switch; Redox probe; Ethanol.

1. Introduction

Active components in nanometric functional structures are often low dimensional materials, such as nanoparticles, nanowires (NWs) and/or films, assembled following a specific design to achieve new properties or to perform determined functions. In this context, the processing route to obtain the individual components and the final device is of major importance. Among the techniques to produce metallic nanostructures, electrodeposition has proven to be a simple, efficient, and low-cost route to obtain these materials. In the case of NWs, template-assisted electrocrystallization methods offer the advantage of controlling key geometrical parameters such as their diameter and length. in addition to the center-to-center distance, and the regularity of the NWs distribution in the array.

Metallic NWs are widely used in sensing [1] and electrocatalysis [2] platforms because of their large area-to-volume ratio, the versatility in tailoring the material's composition and their excellent electrical conductivity. Electrodes may be then designed for distinct applications by densely covering a surface with disordered NWs (free from the template), by using the NWs immersed in carbon paste, or by keeping the NWs inside the template pores, conforming an ordered array which is attached to the electrode plate. To maximize the electrode exposed (active) area, a modular nanostructure may be conceived in which an ordered array of template-free NWs stands perpendicularly attached to a continuous layer, the later acting as the electrode basis. When these 'nanobrushes' are made up of one or more ferromagnetic materials ─besides becoming easily recoverable for re-use─ new design variables appear.

It is well known [3] that magnetic properties are strongly influenced by the material microstructure (phases and their volume distribution, grain size, etc.) and by the nanomagnet size and shape (geometrical characteristics). In nanobrushes, two low-dimensional nanostructures (wire and thin film geometries) are brought together, therefore the magnetic response of this hybrid structure can be tailored to specific purposes by controlling the constitutive materials and geometry [4].

An enhanced magneto-impedance (MI) effect has been reported in magnetic conductive systems based on nanobrushes, such as Co NWs grown in Anodized Aluminum Oxide (AAO) templates with a FeNi [5] or FeCo [6] thin film on the top. These contributions explain the relatively large improvement observed in MI based on different transverse magnetic moment distributions, induced by the exchange interaction of magnetic moments trough the interface between the NWs and the film. However, the mechanism by which the exchange coupling modifies MI remains unclear. According to an extensive bibliographic search, to the best of our knowledge there is no record of properties characterization nor of practical applications of magnetic pure metallic NWs attached to a top layer of the same material.

Diverse nickel-containing nanomaterials have been employed for electrochemical applications due to nickel's high intrinsic efficiency as oxidation reaction enhancer for many compounds, such as alcohols, carbohydrates and other organic molecules, in alkaline media [7-10]. When Ni NWs with high aspect ratio are grown, shape anisotropy becomes dominant in the total anisotropy equation at room temperature, and the magnetic easy axis (EA) lies near the NWs' long axis direction [11-23]. Competing with this preferential spontaneous magnetization direction, the magnetic anisotropy of a film promotes the magnetization to lay on its plane. Hence, when these two morphologies are brought in mutual contact (conforming the Ni nanobrush), the interplay of these two competing anisotropies is the responsible ─to a large extent─ of the resulting EA orientation. When an external magnetic field is applied to this platform, with different magnitudes and/or relative orientations, not only changes in the magnetic response of the whole system may be expected but also in the global platform morphology, likewise affecting the device performance. This latter phenomenon may be exploited for designing magnetic-controlled switches.

In this article, the effects of applying a low uniform magnetic field on the nanobrush morphology and magnetic behavior are investigated. Microstructures and magnetic hysteresis properties are characterized and the effect of a small external magnetic field on the platform morphology and performance are further explored for two well-known redox probes, such as potassium ferricyanide and ethanol.

2. Experimental details

Ultrapure (99,997%) aluminum disks (Alfa Æsar), ethanol absolute anhydrous (99.88%), sodium borate and sodium hydroxide (J. T. Baker), Oxalic, phosphoric and hydrochloric acids**,** together with copper (II) chloride, chromium (III) oxide**,** potassium iodide, iodine and nickel (II) chloride hexahydrate (98%) (Sigma-Aldrich) were used to prepare the alumina templates and to perform the electrodeposition. All the solutions were prepared with ultrapure water (ρ = 18.0 MΩ·cm) obtained from a Millipore-MilliQ equipment. The supporting electrolytes for the electrochemical measurements were NaOH 0.100 mol L^{-1}, 0.100 mol L^{-1} borate buffer solution pH 8.30 and 0.100 mol L^{-1} phosphate buffer solution pH 7.40, respectively. The experiments were all conducted at room temperature.

Ni NW arrays were synthesized by direct current (DC) electrodeposition of Ni into 55 nm diameter cylindrical pores of an alumina AAO template [24], grown by a two-step anodization technique, as described elsewhere [4]. Briefly, ultrapure aluminum disks, 2 cm in diameter and 0.2 mm thick were used as starting material to prepare nanoporous alumina templates. After cleaning and electropolishing the

Al substrate, a first anodization step in oxalic acid was performed at 40 V, at 2 ºC for 4 h. Then, the oxide layer was removed with a chromic acid solution and a second anodization step was performed under the same conditions than the first one, for 20 h. The diameter of the pores d_{pore} and the mean center-to-center distance between adjacent pores, *dcc*, are determined by the anodization voltage, whereas the template's thickness *L* depends on the time of the second anodization. For the mentioned working conditions, d_{anod} = (40±5) nm, *dcc*=(110±10) nm and *L*=35 μm.

Prior to Ni electrodeposition, the bottom of the aluminum template was removed with a copper (II) chloride in hydrochloric acid solution. The remaining alumina closing the pores at the bottom acts as a barrier layer reducing conductivity, so it was thinned by etching with phosphoric acid; in this process, pore diameter enlargement also takes place, changing from d_{anod} to d_{pore} = (55±5) nm, without varying the center-to-center distance. Finally, a 200 nm thick gold layer was sputtered on the bottom of the template to close one end of the pores and to provide a good electrical contact.

The synthesis route to obtain a Ni nanobrush is illustrated in the scheme of Figure 1. Starting from the AAO template, the pores are first partially filled by DC electrodeposition with Ni ions coming from an aqueous solution used as electrolyte in a three-electrode cell; this produces the Ni NWs array. If the process is not stopped before a critical time (which depends on the template size and the synthesis characteristics) the template is then overfilled and a nickel film grows over the Ni NWs [25].

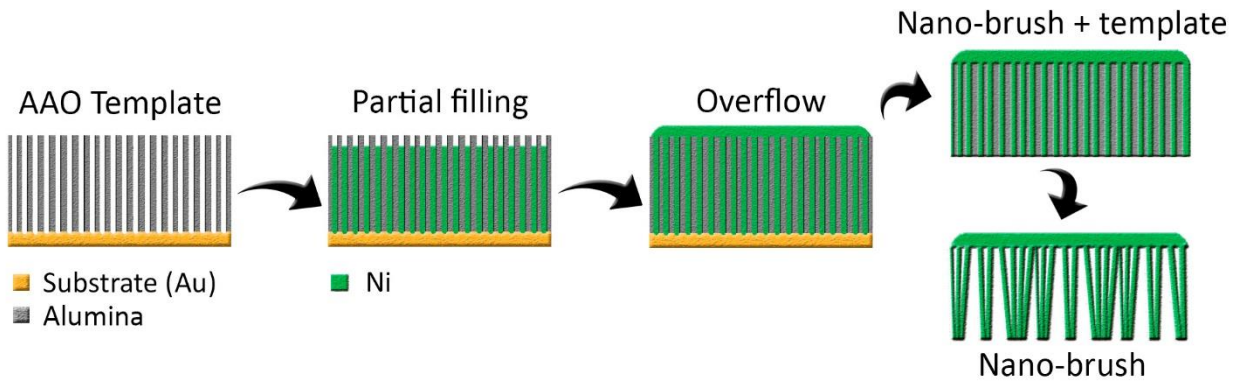

Figure 1. Scheme showing the synthesis path of the Ni nanobrush.

During the electrodeposition process, the current remains almost constant in a first stage in which the pores are filling; when the metal overflows, the current intensity starts to increase, and becomes somewhat irregular (data not shown). The critical time to completely fill a template, using an electrodeposition potential of -1.2 V vs. Ag/AgCl, is approximately 20 minutes. The process continues for

100 additional minutes, to ensure the growth of a uniform top layer, which can provide mechanical stability to the platform. The (gold) substrate used as working electrode during the synthesis is then dissolved in a 0.10 mol L^{-1} I_2 + 0.70 mol L^{-1} KI solution, keeping Ni and Al_2O_3 unaltered. The electrodeposited area is a circle 1 cm in diameter (D = 1 cm).

A Sigma Zeiss Field Emission-Scanning Electron Microscope (FE-SEM), with an Oxford Energy Dispersive Spectrometer (EDS) was used to determine the samples' morphology and to estimate the chemical composition. Crystalline structure and texture were determined by X-ray diffraction (XRD) in a Philips PW 1800/10 diffractometer, with Cu $K\alpha$ radiation (λ = 1.540 Å).

Room temperature magnetic hysteresis loops were measured in a vibrating sample magnetometer (VSM) Lakeshore 7300 at room temperature, applying a maximum magnetic field $\mu_0 H_{max}$= 1.3 T, which was enough to saturate the samples. Major hysteresis loops were measured for different values of the angle θ between the applied magnetic field H and the NWs long axis, varying from 0° to 90°, at 15° steps. Coercivity and relative magnetization were then determined for each orientation.

The magnetic field applied during electrochemical experiments was generated by Helmholtz coils, providing a homogeneous field of 6 mT in a relatively large spatial region as compared to the system dimensions. The electrochemical cell was placed inside the Helmholtz coils in a manner to provide a magnetic field parallel to the Ni NWs long axis direction (normal to the electrode plane).

Electrochemical experiments ─cyclic voltammetry (CV), electrochemical impedance spectroscopy (EIS) and electrochemical capacitance spectroscopy (ECS)─ were performed with an Autolab PGSTAT 30 potentiostat equipped with an ADC750 and a frequency response analyzer (FRA) hardware module and software. The electrochemical experiments were conducted using the Ni nanobrush as working electrode, an Ag/AgCl/NaCl reference electrode and a platinum wire counter-electrode from CH Instruments. Prior to every single electrochemical assay, the working electrodes were pre-treated by performing 10 cycles in the potential window from -0.200 V to 0.800 V, in a NaOH 0.100 mol L^{-1} solution.

EIS experiments were performed in the frequency range from 10 kHz to 10 mHz, using 10 mV as a potential perturbation and 0.200 V and 0.550 V as working potentials, being the redox markers 2.0 x 10^{-3} mol L^{-1} $[Fe(CN)_6]^{4-/3-}$ and ethanol 0.050 mol L^{-1}. The impedance spectra were analyzed using the Z-view software. Electrochemical Capacitance Spectroscopy experiments (ECS) with alternating current (AC) frequencies ranging from 1 MHz down to 10 mHz, with an amplitude of 10 mV (peak to peak), were acquired at the stationary potentials of 0.000 V and 0.600 V. All the obtained impedance data were tested in compliance with the constraints of Kramers−Kronig linear systems theory through an appropriate

routine of the FRA Autolab software. The complex impedance function, $Z^*(\omega)$, was converted into complex capacitance, $C^*(\omega)$, through the physical definition $Z^*(\omega) = 1/j\omega C^*(\omega)$ in which ω is the angular frequency and $j = \sqrt{-1}$. From this conversion, note that the imaginary component of complex capacitance is $C'' = \varphi Z'$ and the real component of complex capacitance is $C' = \varphi Z''$, where $\varphi = (\omega|Z|^2)^{-1}$ and $|Z|$is the modulus of Z^*. All measurements were carried out at room temperature.

3. Results and discussion

3.1. Morphology

Figure 2.a displays a SEM image of the nanobrush platform after dissolving the AAO template, in which the Ni NWs and a 10 µm thick top layer can be seen. The top layer exhibits a rather rough surface which is adhered to the Ni NWs.

After the complete removal of the Ni nanobrush from the AAO template, the Ni NWs no longer stand with a parallel alignment and lose mechanical strength due to their large aspect ratio. The free wire ends agglomerate while still staying attached to the top layer. As a result of this, the platform acquires a pyramidal-like clustered structure, which is possible to observe using a laser confocal microscope, as shown by the top view image of Figure 2.b. When a small magnetic field is applied perpendicularly to the film, the clusters open up as a consequence of the individual Ni NWs alignment with the external field. These details can be observed in Figure 2.c and 2.d, where lateral views of the nanobrush are displayed without and with an applied magnetic field, respectively.

For structural and magnetic characterization, the Ni nanobrush was kept as-prepared in the AAO template. Since the AAO template is diamagnetic, with a magnetic signal much smaller and clearly distinguishable from that of the ferromagnetic Ni NWs, the whole system can be studied from the magnetic point of view. For electrochemical characterization the AAO template was completely removed by immersing it in chromic acid at room temperature for two days.

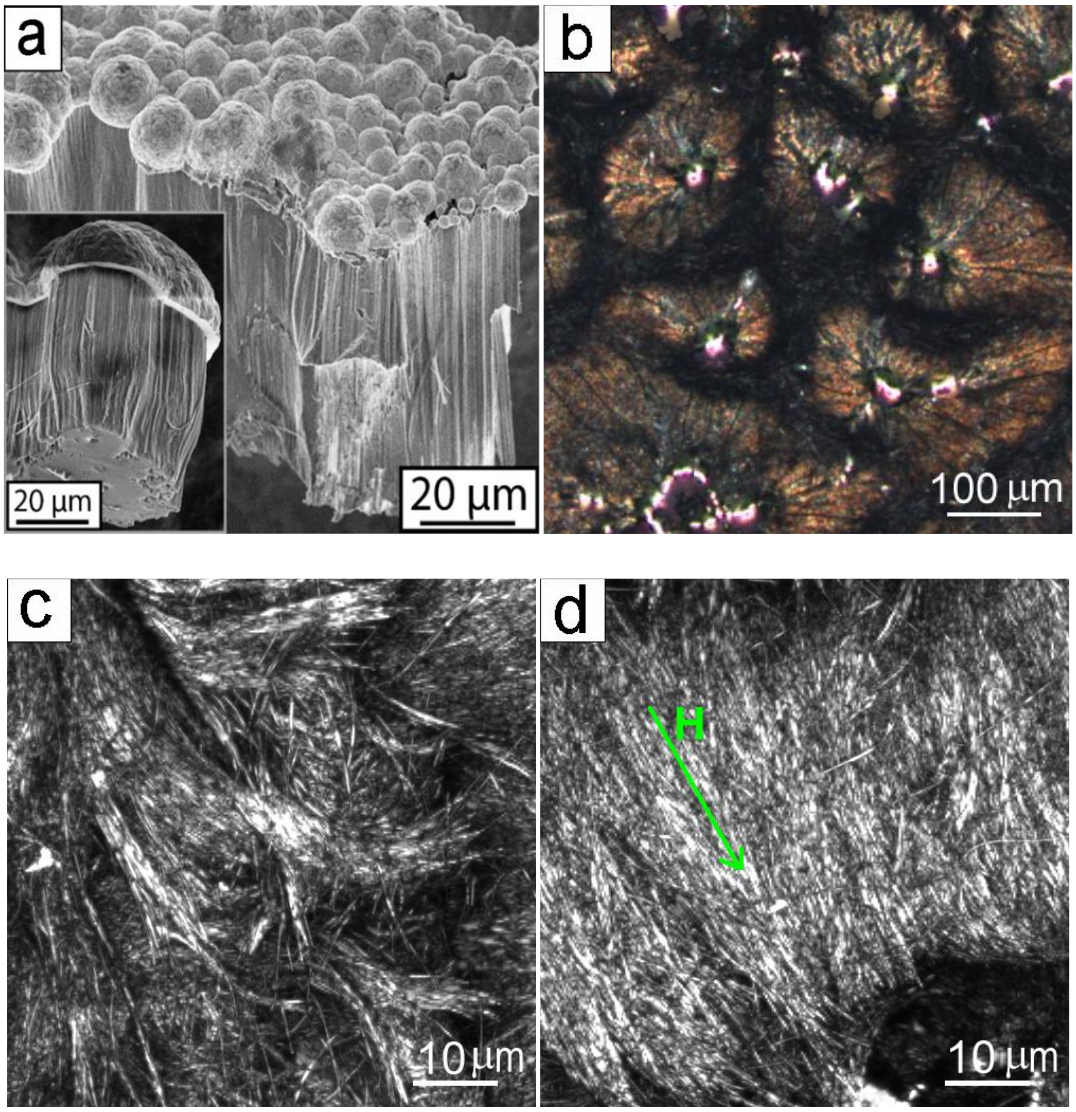

Figure 2. (a) SEM image of the nanobrush after dissolving the AAO template. (b) Confocal image (top view) of the nanobrush where the formation of small "pyramidal-like" NWs agglomerates of the individual Ni NWs is clearly visible. Confocal lateral views of the nanobrush (c) without and (d) with applied magnetic field, in the direction shown by the arrow. The alignment of the individual NWs with the field is evident.

3.2. Crystalline structure

The crystalline structure of the Ni nanobrush was investigated by XRD analysis, measuring both the upper layer and the Ni NWs section of the Ni nanobrush. Figure 3 shows the XRD patterns obtained from both surfaces.

A cubic *fcc* crystalline single phase is noticed in both surfaces with the same lattice constant a = (3.526±0.003) Å, in agreement with Ni pattern (PDF #00-004-0850). A mean crystallite size of 20 nm

was estimated for both, the top layer and the Ni NWs, with the Scherrer formula. As shown in Figure 3, diffraction peaks corresponding to the Ni NWs display different relative intensities, as compared to the standard pattern, due to a strong crystallographic texture along the (220) direction. This preferential apparent texture may arise from small grains forming the Ni NWs which grow preferably with the (220) plane normal to the wires' axis. On the other hand, the top Ni layer shows only a slight preference for the (220) direction, denoting a rather isotropic grain orientation.

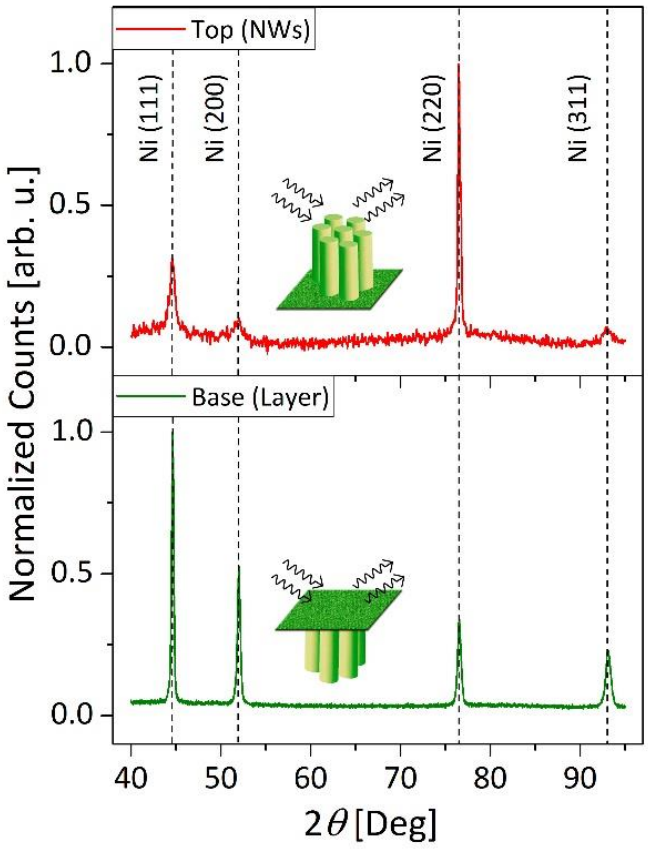

Figure 3. XRD patterns obtained for both surfaces of the Ni nanobrush. The AAO template was kept for the measurement on the NWs side, in order to have perpendicular incidence of the beam with respect to the NWs axis.

3.3. Magnetic Properties

The normalized magnetic moment *m* (defined as the magnetic moment divided by its saturation value) as a function of the applied magnetic field *H* is found to saturate at a much higher field in the PA configuration (field applied parallel to the NWs axis) than in the PE field orientation (field applied

perpendicular to the NWs axis). Coercivity (the applied field at which $m = 0$) is also higher in the former configuration, as illustrated in Figure 4.a, in a close-up of the low-field region of the loops.

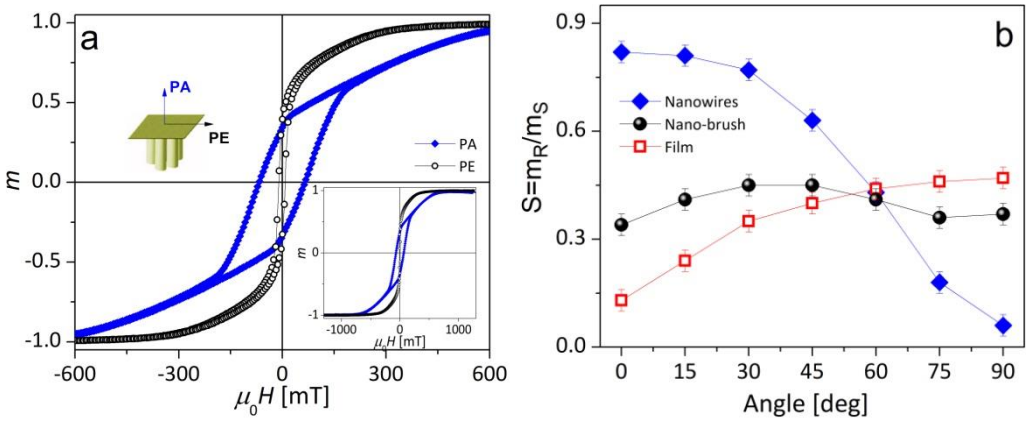

Figure 4. a) Low field region of the hysteresis loops measured at room temperature, with the field applied in PA and PE configurations (refer to the scheme in the figure). The inset in the right bottom corner displays the major loops in the full measurement range. b) Squareness S (= m_R/m_S) corresponding to the NWs array (blue diamonds), to the detached film (red open squares) and to the complete platform (black spheres), showing the angular position of the effective easy axis (maximum in S) for each configuration.

The difference in the magnetic behavior between PA and PE configurations arises from to the complex brush geometry, which makes it difficult to estimate the actual internal field for the different orientations, besides the non-uniform crystalline texture distribution in the brush, as reveled by XRD measurements. These two factors largely affect the magnitude of the effective anisotropy and the resulting easy axis (EA) direction of the platform, and so the loop shape and the values of hysteresis parameters when the magnetic field is applied in different directions. The angular dependence of the squareness S (= m_R/m_S with m_R the remanent magnetization) provides information about the actual orientation of the effective EA of the magnet, which is aligned near the angle at which S has a local maximum [26, 27]. The dependence of S on the angle θ between the external applied field and the NWs long axis is shown in Figure 4.b for the separate components: the layer, the NWs and for the whole platform. As expected, $\theta = 0$ is the hard axis for the layer while this direction is the natural EA for the long-aspect-ratio NWs array. Regarding the complete platform, a small maximum is observed near $\theta \approx 35°$ indicating that its effective EA points near this out-of-plane direction.

The total moment measured in the Ni nanobrush results from the contributions of both, the 10 μm thick layer and the Ni NWs. Regarding the shape anisotropy contribution to the effective anisotropy, it arises from the interplay/competition of an EA parallel to the NWs long axis (PA direction) and an EA

parallel to the plate plane (PE), which are orthogonal. When the crystallographic texture is also considered, this magnitude is quite low in the plate indicating that grains are almost isotopically oriented. On the other hand, the strong (220) texture in the NWs along the major axis direction indicates that the crystallographic EA (111) directions corresponding to the *fcc* structure are on the surface of a cone of semi aperture of about 35° from the axial direction. This NWs off-axis contribution to the effective anisotropy seems to compete with the previously described contributions; a detailed description of these effects was published elsewhere [4].

3.4. Electrochemical characterization of the Ni nanobrush

In order to evaluate the electrochemical behavior and to determine the electrocatalytic activity of Ni species originated at Ni NWs, as part of the Ni nanobrush system, cyclic voltammograms (CV) experiments were done, using this platform as a working electrode. For this purpose, the working electrode was initially pre-treated performing 10 subsequent scan potential cycles between -0.200 V and 0.800 V, in NaOH 0.100 mol L^{-1}, as was previously determined for Ni nanostructured electrodes [8]. Figure 5 depicts the CV responses.

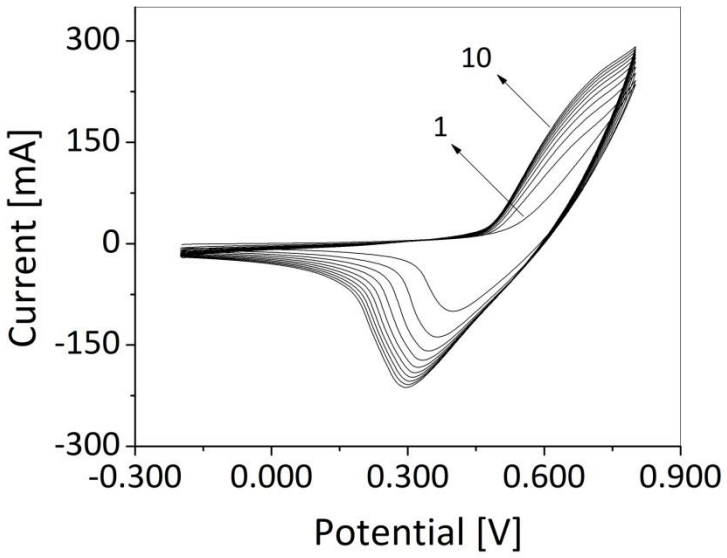

Figure 5. Consecutive cyclic voltammograms for the Ni nanobrush platform. Supporting electrolyte: 0.100 mol L^{-1} NaOH. Scan rate: 0.100 V s^{-1}.

It may be observed in Figure 5 that there is no evidence of anodic processes from the first cycle, while a small cathodic response may be detected in the reverse scan. In the subsequent cycles, an incipient anodic signal appears and the reduction current signal becomes more important as the number of cycles increases. A spontaneously-formed small amount of $Ni(OH)_2$ initially appears when the Ni NWs surface is placed in contact with an alkaline aqueous solution [8, 28, 29], as described by the following equation:

$$Ni_{(s)} + 2\,OH^-_{(ac)} \rightleftharpoons Ni(OH)_{2(s)} + 2\,e^- \qquad (1)$$

Once the potential of the working electrode is scanned, the small amount of $Ni(OH)_2$ produced after the first cycle is not enough to provide a detectable electrochemical oxidation current [8], but this is accomplished after the 10th cycle. The processes taking place on the working electrode may be described by considering that in the first cycle, both Ni (0) oxidation and $Ni(OH)_2$ (Ni (II)) production processes (Eq. 1 and Eq. 2 below) occur at higher potentials than the oxidation step of $Ni(OH)_2$ to form NiOOH (Ni(II) to Ni(III)), which starts to be evident in the second cycle.

$$Ni(OH)_{2(s)} + OH^-_{(ac)} \rightleftharpoons NiOOH_{(s)} + H_2O_{(l)} + e^- \qquad (2)$$

As a result of this, the cathodic current peaks obtained along the CV experiment, from the first to the tenth cycle, are due to the reduction process of NiOOH to restore $Ni(OH)_2$ at the working electrode surface (Eqn. 2).

After this pre-treatment to maximize the presence of NiOOH catalyst, further experiments were performed by Electrochemical Impedance Spectroscopy (EIS) for characterizing the electronic behavior of the Ni nanobrush as working electrode. Taking advantage of the ferromagnetic properties of the Ni nanobrush, the system electrochemical response was evaluated under and without the influence of a relatively small external magnetic field $\mu_0 H$= 6 mT**,** applied parallel to the Ni NWs long axis (normal to the layer plane/electrode surface).

It is important to remark that large magnetohydrodynamical effects associated with the Lorentz's force acting on the carrier ions due to the external magnetic field *H* are actually small, since the electric field generated between the electrodes is mainly perpendicular to this applied magnetic field, at least far from the electrode**.** Nearby the conducting, ferromagnetic nanobrush surface, electric and magnetic fields may locally bend and net forces on the charges may appear; these perturbations are disregarded in the following analysis.

Another effect of the external magnetic field is the magnetostatic Zeeman interaction with the platform. As the Ni NWs are ferromagnetic, the magnetic torque applied by the external field ***H*** tries to align them

parallel to it, thereby opening the clusters observed in Figure 2.b. The effect of an external magnetic field on the nanowires orientation is shown in Figures 2.c and 2.d.

The electrochemical response of the platform in the presence of the external magnetic field was further explored with impedance spectroscopy techniques. Figure 6.a displays Nyquist plots obtained at 0.200 V for 2.0 x 10^{-3} mol L^{-1} $[Fe(CN)_6]^{4-/3-}$ in 0.100 mol L^{-1} borate buffer pH 8.30 as supporting electrolyte solution, measured under and without the influence of an applied magnetic field. The experimental data were fitted with a ($R_s(R_{ct}C_{dl})$) circuit (where R_s is the electrolytic resistance, R_{ct} the charge-transfer resistance and C_{dl} the double layer capacitance). From the analysis of the experimental R_{ct} values, an improvement in the electrochemical response towards $[Fe(CN)_6]^{4-/3-}$ was found when the magnetic field was applied, which is clear from the R_{ct} value of (17.5 ± 0.2) kΩ for the Ni nanobrush under magnetic field, being (22.7 ± 0.4) kΩ without the influence of ***H***. Therefore, the redox marker undergoes a facilitated electron transfer process in presence of the magnetic field, improving the electrochemical response. This fact is even more noticeable when the magnetic field is removed, since the R_{ct} values increase, returning to the initial conditions (data not shown), demonstrating that the magnetic control enhances the charge transfer of the redox probe, generates a higher electroactive area by ordering/aligning the Ni NWs on the surface of the nanobrush, and provides a more reactive surface towards the electrochemical probe.

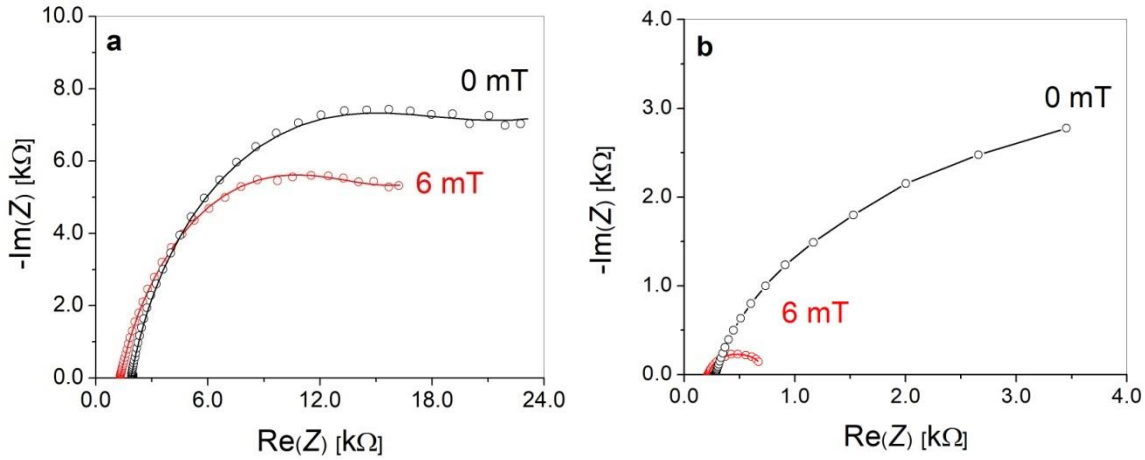

Figure 6. Nyquist plots for the impedance spectra of the Ni nanobrush measured without (black, 0 mT) and under (red, 6 mT) an applied magnetic field. Open circles are experimental data and solid lines correspond to a ($R_s(R_{ct}C_{dl})$) circuit model (with R_s the electrolytic resistance, R_{ct} the charge-transfer resistance and C_{dl} the double layer capacitance). Frequency range: 10 kHz to 10 mHz, potential perturbation: 0.010 V. (a) Working electrode potential: 0.200 V in 2.0 x 10^{-3} mol L^{-1} $[Fe(CN)_6]^{-4/-3}$. Supporting electrolyte: 0.100 mol L^{-1} borate buffer pH 8.3. (b) Working electrode potential: 0.550 V. Ethanol solution: 0.050 mol L^{-1}. Supporting electrolyte: 0.100 mol L^{-1} NaOH.

To obtain complementary information, an additional assay to test the oxidation response for ethanol at 0.550 V was performed, comparing the behavior of the Ni nanobrush under and without magnetic field (Figure 6.b). In this case, ethanol is used as redox probe to highlight the effect of magnetic control on the electroactivity of the Ni nanobrush. To accomplish this purpose, the electrode surface was pre-treated as it was described before (10 cycles of scan potential in 0.100 mol L^{-1} NaOH) allowing the formation of $Ni(OH)_2$ and NiOOH, to increase the electrocatalytic layer and make the surface responsive to ethanol oxidation. Figure 6.b displays the resulting Nyquist plots obtained at 0.550 V for 0.050 mol L^{-1} ethanol in 0.100 mol L^{-1} NaOH as supporting electrolyte solution, under and without magnetic field. The experimental data were fitted using the same equivalent electrical circuit previously described. From the analysis of EIS experiments, the R_{ct} value found for the Ni nanobrush without magnetic field was (5.1 ± 0.3) kΩ, while an important decrease (around 10 times) was observed for the R_{ct} under the influence of H (0.496 ± 0.007) kΩ. The decrease of R_{ct} observed for ethanol when a magnetic field is applied is more pronounced than the one found for $[Fe(CN)_6]^{4-/3-}$ under the same conditions. The results allow to conclude that the magnetic field leads to a more efficient electrocatalytic activity of the Ni nanobrush surface towards ethanol, by increasing the electro-catalyzer effective area through separation/alignment of the Ni NWs by the magnetic force.

To further investigate and obtain additional information on the electrochemical behavior of the Ni nanobrush and to correlate it with EIS results, Electrochemical Capacitance Spectroscopy (ECS) analyses were performed. Electrochemical capacitance spectroscopy (ECS) is an impedance-derived spectroscopic (time- or frequency-dependent) method that allows determining the capacitance associated to molecular quantum states and mesoscopic electrochemical systems in general [30-34]. ECS is based on impedimetric measurements, where the complex impedance, $Z^*(w)$ is converted into a complex capacitance, $C^*(w)$. Thus, the ECS approach provides an electroanalytical signal (at low frequency) that is purely capacitive, owing to the assessment of the electronic states of the Ni nanobrush. For the system under study, an electrochemical impedance-derived capacitance spectroscopic approach is a powerful tool to evaluate the influence of the applied magnetic field on the electronic density of states and its contribution to the electrochemical capacitance of the Ni nanobrush. Figure7 displays the capacitance results obtained from EIS experiments at two different potentials.

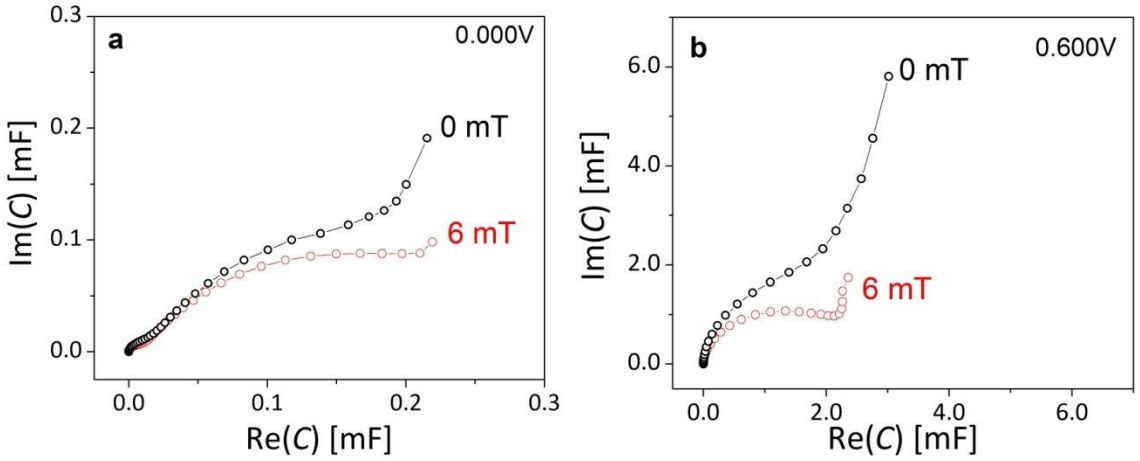

Figure 7. Capacitive Nyquist diagrams obtained for Ni NWs at 0.100 mol L^{-1} phosphate buffer pH 7.40 without (black, 0 mT) and under (red, 6 mT) applied magnetic field. Frequency range: from 1 MHz to 0.01 Hz; amplitude: 10 mV; (a) working potential: 0.000 V and (b) working potential: 0.600 V.

The EIS spectra were obtained at stationary potentials of 0.000 V (Figure7.a) and 0.600 V (Figure7.b) vs Ag/AgCl/NaCl electrochemical reference electrode, for frequencies ranging from 1 MHz down to 10 mHz with a peak-to-peak amplitude of 10 mV. The stationary potentials were selected from the CV experiments under different conditions: (a) 0.000V, where no faradaic processes occur and (b) 0.600 V, the optimal potential to promote the oxidation processes described in Eqs. (1) to (3), considering that the molecular (quantum) capacitance of the Ni nanobrush is expected to be maximum, unlike at 0.000 V. For the selected working conditions, it can be observed that for both potentials, the electrochemical capacitance increases under a magnetic field, confirming that the Ni NWs in the nanobrush tend to be arranged in an upright position, parallel to each other and to the applied field ***H*** (as shown in Figure 2.d). As expected, this effect is highly magnified when the potential is increased to 0.600 V (Figure 6.b), demonstrating an important correlation with EIS results.

4. Conclusion

Ni nanobrushes (aligned NWs connected by a top layer of the same material) were synthesized in one step by DC electrodeposition into AAO templates. The resulting NWs are polycrystalline, with small (20 nm) crystallite size and exhibit a strong (220) crystallographic texture in the long axis direction. On the contrary, the film only displays a slight texture in that direction, which is normal to its own surface. Nanobrushes are ferromagnetic, with a shape- and texture-controlled effective easy axis orientation.

When a constant and uniform magnetic field *H* is applied in the NWs soft direction (NWs easy axis) a more efficient catalytic activity and an enhanced electrochemical response of the Ni nanobrush surface towards ethanol and $[Fe(CN)_6]^{4-/3-}$ is observed. This behavior is then attributed to the increase of the

effective area for the catalytic reaction when *H* is applied, mainly due to the tendency of the Ni NWs to align with the external magnetic field. In fact, NWs tend to deagglomerate from the original clusters, increasing the Ni exposed area. The improvement in the electrochemical capacitance in presence of the applied magnetic field is also consistent with a new configuration of the Ni NWs, in which they are more separated, leading to a larger electrode active area. This effect appears magnified at a higher potential of 0.600 V, evidencing an indirect magnetic control on the electroactivity of this platform, by an efficient enhancement of the response towards the redox probes assayed. This effect could be potentially applied for the fabrication of an on/off switch in electrochemical detection platforms.

Conflicts of interest

The authors declare that they have no known competing financial interests or personal relationships that could have appeared to influence the work reported in this paper.

Acknowledgments

This work has been partially funded by Secyt-UNC (PROYECTOS CONSOLIDAR 2018-2021 - Codes: 33620180100198CB01 and 33620180100433CB), Conicet, and ANPCyT (PICT-2015-0077, PICT-2018-01177). F. M. acknowledges a CONICET fellowship.

Data availability

The raw and processed data required to reproduce these findings are available upon request to the corresponding author.

References

[1] J. Wang, Z. Li, Z. Gu. A comprehensive review of template-synthesized multicomponent nanowires: From interfacial design to sensing and actuation applications, *Sensors and Actuators Reports* 3 (2021) 100029. DOI: 10.1016/j.snr.2021.100029.

[2] W. Wang, F. Lv, B. Lei, S. Wan, Mi. Luo, S. Guo. Tuning Nanowires and Nanotubes for Efficient Fuel-Cell Electrocatalysis, *Advanced Materials* (2016) 1-25. WILEY-VCH Verlag GmbH & Co. KGaA, Weinheim. DOI: 10.1002/adma.201601909.

[3] R. C. O'Handley, Modern magnetic materials: Principles and Applications. 2000, John Wiley and Sons, New York.

[4] F. Meneses, P. G. Bercoff in *Advances in Nanotechnology*. Vol. 24, Ch. 7. Magnetic and Electric Characterization of Different Ni Systems Comprising Cylindrical Nanowires. (2020) 219-278. ISBN: 978-1-53618-599-7 (eBook).

[5] Y. Zhang, J. Dong, X. Sun, Q. Liu, J. Wang. Interface coupling-induced enhancement of magnetoimpedance effect in heterogeneous nanobrush by adjusting textures of Co nanowires, *Nanoscale Research Letters*, Vol. 8, No. 1 (2013) 471.

[6] Y. Ren, Y. Dai, B. Zhang, Q. Liu, D. Xue, J. Wang. Tunable magnetic properties of heterogeneous nanobrush: from nanowire to nanofilm, *Nanoscale Research Letters*, Vol. 5, No. 5 (2010) 853.

[7] M. Fleischmann, K. Korinek, D. Pletcher. The oxidation of organic compounds at a nickel anode in alkaline solution, *J. Electroanalytical Chem*. 31 (1971) 39–49. doi:10.1016/S0022-0728(71)80040-2.

[8] C. S. Tettamanti, M. L. Ramírez, F. A. Gutierrez, P. G. Bercoff, G. A. Rivas, M. C. Rodríguez. Nickel nanowires-based composite material applied to the highly enhanced non-enzymatic electro-oxidation of ethanol, *Microchemical Journal*, Vol. 142 (2018) 159-166.

[9] B. Wang, S. Li, J. Liu, M. Yu. Preparation of nickel nanoparticle/graphenecomposites for non-enzymatic electrochemical glucose biosensorapplications, *Mat. Res. Bull.* 49 (2014) 521–524. doi:10.1016/j.materresbull.2013.08.066.

[10] S. Majdi, A. Jabbari, H. Heli, A. A. Moosavi-Movahedi. Electrocatalytic oxidation of some amino acids on a nickel-curcumin complex modified glassy carbon electrode, *Electrochim. Acta*. 52 (2007) 4622–4629. doi:10.1016/j.electacta.2007.01.022.

[11] A. Kumar, S. Fähler, H. Schloerb, K. Leistner, L. Schultz. Competition between shape anisotropy and magnetoelastic anisotropy in Ni nanowires electrodeposited within alumina templates, *Phys. Rev. B*, Vol. 73, No. 6 (2006) 064421.

[12] H. Zeng, S. Michalski, R. Kirby, D. Sellmyer, L. Menon, S. Bandyopadhyay. Effects of surface morphology on magnetic properties of Ni nanowire arrays in self-ordered porous alumina, *Journal of Physics: Condensed Matter*, Vol. 14, No. 4 (2002) 715.

[13] F. Tian, Z. Huang, L. Whitmore. Fabrication and magnetic properties of Ni nanowire arrays with ultrahigh axial squareness, *Physical Chemistry Chemical Physics*, Vol. 14, No. 24 (2012) 8537-8541.

[14] R. Lavin, J. Denardin, A. Espejo, A. Cortés, H. Gómez. Magnetic properties of arrays of nanowires: Anisotropy, interactions, and reversal modes, *J. of Applied Physics*, Vol. 107, No. 9 (2010) 09B504.

[15] R. Lavin, J. C. Denardin, J. Escrig, D. Altbir, A. Cortés, H. Gómez. Angular dependence of magnetic properties in Ni nanowire arrays, *J. of Applied Physics*. 106 (2009) 103903. doi: 10.1063/1.3257242J.

[16] M. Vázquez, K. Pirota, J. Torrejón, D. Navas, M. Hernández-Vélez. Magnetic behavior of densely packed hexagonal arrays of Ni nanowires: Influence of geometric characteristics, *J. Mag. Magn. Mat*, Vol. 294, No. 2 (2005) 174-181.

[17] R. Hertel. Micromagnetic simulations of magnetostatically coupled Nickel nanowires, *J. of Applied Physics*, Vol. 90, No. 11 (2001) 5752-5758.

[18] K. Nielsch, R. Wehrspohn, J. Barthel, J. Kirschner, U. Gösele, S. Fischer, H. Kronmüller. Hexagonally ordered 100 nm period nickel nanowire arrays, *Applied Physics Letters*, Vol 79, No. 9 (2001) 1360-1362.

[19] C. Han, S. Yang, K. Chang, P. Wang, R. Murakami, X. Song. Structure transition and magnetism of bcc-Ni nanowires, *J. of Mater. Chemistry C*, Vol. 3, No. 5 (2015) 1004-1010.

[20] J. De La Torre Medina, G. Hamoir, Y. Velázquez-Galván, S. Pouget, H. Okuno, L. Vila, A. Encinas, L. Piraux. Large magnetic anisotropy enhancement in size-controlled Ni nanowires electrodeposited into nanoporous alumina templates, *Nanotechnology*, Vol. 27, No. 14 (2016) 145702.

[21] N. Biziere, C. Gatel, R. Lassalle-Balier, M. C. Clochard, J. E.Wegrowe, E. Snoeck. Imaging the fine structure of a magnetic domain wall in a Ni nanocylinder, *Nano Letters*, Vol. 13, No. 5 (2013) 2053-2057.

[22] H. Hwang, C. Kim, Y. Jang, J. Cho, S. Bhang, H. Moon. Effect of annealing on the magnetic properties of Ni nanowires prepared by using an anodized aluminum oxide template, *J. of the Korean Physical Society*, Vol 58, No. 31 (2011) 654-658.

[23] F. Meneses, S. E. Urreta, J. Escrig, P. G. Bercoff. Temperature dependence of the effective anisotropy in Ni nanowire arrays, *Current Applied Physics*, Vol. 18, No. 11 (2018) 1240-1247.

[24] H. Masuda, K. S. Fakuda. Ordered Metal Nanohole Arrays Made by a Two-Step Replication of Honeycomb Structures of Anodic Alumina, *Science* 268 (1995) 1466-1468.

[25] C. Schönenberger, B. M. I. van der Zande, L. G. J. Fokkink, M. Henny, C. Schmid, M. Kruger, A. Bachtold, R. Huber, H. Birk, U. Staufer. Template Synthesis of Nanowires in Porous Polycarbonate Membranes: Electrochemistry and Morphology, *J. Phys. Chem. B* 1997, 101, 5497-5505.

[26] S. Gau, C. F. Brucker. Angular variation of the coercivity in magnetic recording thin films, *J. of Applied Physics* 57 (1985) 3988-3990. doi: 10.1063/1.334885.

[27] J-G. Zhu. Coercivity angular dependence in longitudinal thin film media, *J. Mag. Magn. Mat*. 109 (1992) 367-374. doi: 10.1016/0304-8853(92)91775-O

[28] R. S. Schrebler Guzmán, J. R. Vilche, A. J. Arvía. The kinetics and mechanism of the nickel electrode-III. The potentiodynamic response of nickel electrodes in alkaline solutions in the potential region of $Ni(OH)_2$ formation, *Corros. Sci*. 18 (1978)765–778. doi: 10.1016/S0010-938X(78)80094-8.

[29] X. K. Tian, X. Y. Zhao, L. De Zhang, C. Yang, Z. B. Pi, S. X. Zhang. Performance of ethanol electro-oxidation on Ni-Cu alloy nanowires through composition modulation, *Nanotechnology* 19 (2008), 215711. doi: 10.1088/0957-4484/19/21/215711.

[30] P. R. Bueno, G. T. Feliciano, J. J. Davis. Capacitance spectroscopy and density functional theory, *Physical Chemistry Chemical Physics*, 17 (2015) 9375-9382.

[31] D. A. Miranda, P. R. Bueno. Density functional theory and an experimentally-designed energy functional of electron density. *Physical Chemistry Chemical Physics*, 18 (2016) 25984-25992.

[32] P. R. Bueno, F. Fabregat-Santiago, J. J. Davis. Elucidating capacitance and resistance terms in confined electroactive molecular layers, *Analytical Chemistry*, 85 (2013) 411-417.

[33] P. R. Bueno, J. J. Davis. Measuring quantum capacitance in energetically addressable molecular layers, *Analytical Chemistry*, 86 (2014) 1997-2004.

[34] P. R. Bueno, G. Mizzon, J. J. Davis. Capacitance spectroscopy: a versatile approach to resolving the redox density of states and kinetics in redox-active self-assembled monolayers, *Journal of Physical Chemistry* B, 116 (2012) 8822-8829.